

1 **South Georgia in a West Gondwana context: detrital zircon geochronology of**
2 **a late Permian accretionary complex**

3
4

5 **Teal R. Riley¹*, Andrew Carter², Michael J. Flowerdew³, Ian L. Millar⁴, Martin J. Whitehouse⁵**

6
7

¹*British Antarctic Survey, High Cross, Madingley Road, Cambridge, CB3 0ET, UK*

8 *trr@bas.ac.uk*

9 ²*Department of Earth and Planetary Sciences, Birkbeck, University of London, Malet Street, London*
10 *WC1E 7HX, UK*

11 *a.carter@ucl.ac.uk*

12 ³*CASP, Madingley Rise, Madingley Road, Cambridge CB3 0UD, UK*

13 *michael.flowerdew@casp.org.uk*

14 ⁴*British Geological Survey, Keyworth, Nottingham, NG12 5GG, UK*

15 *ilm@bgs.ac.uk*

16 ⁵*Swedish Museum of Natural History, Stockholm, Sweden*

17 *martin.whitehouse@nrm.se*

18
19

20
21 **Author for correspondence*

22 *e-mail: trr@bas.ac.uk*

23

24 **ABSTRACT.** South Georgia lies in a remote position in the circumpolar South Atlantic and is
25 one of the most isolated continental fragments on Earth. The basement geology of South
26 Georgia is restricted to the southeast sector of the island and is termed the Drygalski Fjord
27 Complex, which consists of metasedimentary rocks and localised paragneisses that form an
28 accretionary complex cut by multiple dolerite dykes and gabbroic intrusive rocks. We examine
29 the detrital zircon geochronology and geochemistry of six metasedimentary samples from the
30 Drygalski Fjord Complex to determine their depositional and provenance history and explore
31 correlations to elsewhere in West Gondwana. The basal Salomon Glacier Formation has a
32 maximum depositional age of ca. 270 Ma and a secondary age peak at ca. 470 Ma that is
33 consistent with West Gondwana accretionary complexes from the northern Antarctic
34 Peninsula and Patagonia. This depositional age is also shared with sedimentary successions
35 from the Karoo Basin (South Africa) and East Antarctica, but they lack the secondary age peak
36 (ca. 470 Ma), being instead characterised by an age peak at ca. 530 Ma, associated with the
37 recycled Cambrian sources of East Antarctica. The late Permian accretionary complex of South
38 Georgia is closely correlated to units from the northern Antarctic Peninsula (Trinity Peninsula
39 Group) and the southern Cordillera Darwin, and we favour a common origin on the Antarctic
40 Plate before closure of the Rocas Verdes Basin and translation to the Scotia Plate.

41
42 *Keywords: Antarctic, provenance, Patagonia, Lu-Hf isotopes*
43

44 **Georgia del Sur en el contexto de Gondwana Occidental: geocronología de circones detríticos de un**
45 **complejo acrecionario del Pérmico tardío.** Georgia del Sur se encuentra en una posición remota del
46 Atlántico Sur circumpolar y constituye uno de los fragmentos continentales más aislados del planeta.
47 La geología del basamento de la isla está restringida al sector suroriental y se conoce como el Complejo
48 Drygalski Fjord, compuesto por rocas metasedimentarias y paragneises localizados que conforman un
49 complejo acrecionario intruido por numerosos diques de dolerita y cuerpos gabroicos. En este estudio
50 analizamos la geocronología y geoquímica de circones detríticos de seis muestras metasedimentarias
51 del Complejo Drygalski Fjord, con el fin de determinar su historia de deposición y proveniencia, así
52 como explorar sus posibles correlaciones con otras regiones de Gondwana Occidental. En la base de
53 este complejo, la Formación Salomon Glacier tiene una edad máxima de deposición de ca. 270 Ma
54 y una población secundaria de circones detríticos de ca. 470 Ma, lo cual es consistente con los
55 complejos acrecionarios de Gondwana Occidental ubicados en el norte de la Península Antártica y
56 Patagonia. Edades de deposición similares se han observado en sucesiones sedimentarias de la
57 Cuenca del Karoo (Sudáfrica) y en la Antártica Oriental; sin embargo, estas últimas carecen de la
58 población de circones de ca. 470 Ma, presentando, en cambio, otra de ca. 530 Ma, asociada a fuentes
59 recicladas del Cámbrico de la Antártica Oriental. El complejo acrecionario Pérmico tardío de Georgia
60 del Sur muestra una estrecha correlación con unidades del norte de la Península Antártica (Grupo de
61 la Península Trinidad) y del sur de la Cordillera Darwin, por lo que consideramos más probable un
62 origen común en la Placa Antártica, previo al cierre de la Cuenca Rocas Verdes y a su posterior
63 traslación hacia la Placa Scotia.

64

65 **1. Introduction**

66

67 South Georgia is a remote island in the South Atlantic Ocean, lying approximately 1700 km
68 east of the southern tip of South America. The island is situated towards the eastern extremity
69 of the North Scotia Ridge (Fig. 1), which defines a transform plate boundary between the
70 South American and Scotia plates (Livermore et al., 1994). The North Scotia Ridge is a long-
71 lived strike-slip system that accommodated oceanic spreading during the opening of the
72 Scotia Sea and consists of several, mostly submerged, continental crustal blocks in a linear

73 chain from Tierra del Fuego to South Georgia. The broad consensus (e.g. Carter et al., 2014;
74 Dalziel et al., 2021; Beaver et al., 2022) is that from at least the Cretaceous until the Eocene,
75 the South Georgia microcontinent was a continuation of the Andean Cordillera until Eocene
76 separation and translation to its current location. Dalziel et al. (2021) highlighted the
77 similarities in sedimentary successions between Tierra del Fuego and South Georgia, and
78 proposed that South Georgia originated in the Staten Embayment (Fig. 1). These correlations
79 are supported by detrital zircon provenance analysis of sedimentary successions from South
80 Georgia, Fuegian Andes and the North Scotia Ridge (Barbeau et al., 2010; Carter et al., 2014;
81 Riley et al., 2019).

82 However, a fundamental problem with a contiguous relationship between Tierra del Fuego
83 and South Georgia during the Late Cretaceous is that analysis of seafloor spreading along the
84 West Scotia Ridge can only accommodate approximately half of the strike-slip translation
85 along the North Scotia Ridge required for the post-Eocene separation between Tierra del
86 Fuego and South Georgia (Eagles, 2010). Dalziel et al. (2021) also acknowledged that the
87 Scotia Sea tectonic history could not fully explain the present-day location of South Georgia
88 and suggested that 'escape tectonics' during the Late Cretaceous along transcurrent faults
89 may have also played a role.

90 One aspect that has not been fully addressed is the paleo-location of South Georgia during
91 the late Palaeozoic–early Mesozoic, prior to the breakup of Gondwana. Eagles (2010) and
92 Eagles and Eisermann (2020) proposed that South Georgia originated within the interior of
93 Gondwana, where it must have had a paleo-location to the east of a 'barrier' of thick oceanic
94 lithosphere between the Falkland Plateau and central Scotia Sea basins. They argued that the
95 main stratigraphic elements of South Georgia's Mesozoic and late Palaeozoic history are

96 ubiquitous throughout West Gondwana and are not uniquely diagnostic. Eagles and
97 Eisermann (2020) suggested that detrital zircon age profiles from mid- to Late Cretaceous
98 sedimentary successions on South Georgia could have been derived from magmatic and
99 recycled sources in South Africa as opposed to the Andean Cordillera.

100 In this work we examine, for the first time, the basement metasedimentary succession of
101 South Georgia to explore potential correlations with South America, Antarctic Peninsula, East
102 Antarctica and South Africa in the late Permian, and to provide a test for a South Georgia-
103 South Africa connection. Six metasedimentary siliciclastic samples from the basement
104 Salomon Glacier Formation and Cooper Island Formation of the Drygalski Fjord Complex were
105 analysed for their detrital zircon U-Pb age population, combined with a subset of Lu-Hf
106 isotope analysis, and calculations of maximum depositional age.

107

108 **2. Geological setting**

109

110 The basement geology of South Georgia is restricted to the southeast sector of the island
111 (Fig. 2) and is composed of two distinct complexes, probably separated by a fault (Macdonald
112 et al., 1987). The Drygalski Fjord Complex was defined by Storey (1983) and is characterised
113 by a suite of highly deformed metasedimentary rocks and paragneisses intruded by multiple
114 mafic plutons, leading to localised hornfels texture. Storey (1983) also highlighted the
115 presence of local migmatite layers associated with paragneisses. The Drygalski Fjord Complex
116 has three spatially distinct metasedimentary successions that can be identified in the Salvesen
117 Range, adjacent to Drygalski Fjord and Cooper Island (Fig. 2): the Salomon Glacier, Novosilski
118 Glacier and Cooper Island formations (Dalziel et al., 2021). The age of deposition of the

119 metasedimentary rocks of the Drygalski Fjord Complex is uncertain, but it is intruded by Early
120 Jurassic plutons (Tanner and Rex, 1979; Curtis et al., 2010), some of which are anatectic
121 (Tanner and Rex, 1979). The basal Salomon Glacier Formation, which is the focus of this study,
122 has been subject to higher grade metamorphism (?Buchan-type) and greater deformation
123 than the Cooper Island and Novosilski formations, and as such may not represent a direct
124 equivalent.

125 To the west of the Drygalski Fjord Complex is the Larsen Harbour Complex (Fig. 2), which
126 is interpreted as an ophiolite sequence consisting of a succession, up to 2 km in thickness, of
127 tholeiitic pillow basalts, massive lavas and intercalated chert, cut by multiple mafic dykes
128 (Mair, 1987). It has also been correlated with the Tortuga and Sarmiento ophiolite complexes
129 of South America (Dalziel et al., 2021). The Larsen Harbour and Drygalski Fjord complexes
130 were together interpreted as a Gondwana margin accretionary complex that was subject to
131 crustal thinning during the Late Jurassic (Mukasa and Dalziel, 1996).

132 The major part of South Georgia is dominated by Lower Cretaceous (Carter et al., 2014)
133 turbidite sequences that were deposited in a back-arc basin setting and are separated from
134 the basement units by the Cooper Bay shear zone (Curtis et al., 2010) (Fig. 2). Two laterally
135 equivalent units are identified, the extensive Cumberland Bay Formation and the more
136 spatially restricted Sandebugten Formation (Fig. 2). The Cumberland Bay Formation is up to 8
137 km in thickness and consists of volcaniclastic greywackes of andesitic composition deposited
138 in a continental margin magmatic arc setting that was deformed into large-scale (>100 m)
139 folds associated with low-grade regional metamorphism. The Cumberland Bay Formation is
140 host to a probable Lower Cretaceous (Aptian) fossil (ichnofauna) assemblage (Macdonald,
141 1982). The adjacent Sandebugten Formation is a more siliciclastic quartz-rich sandstone and

142 shale turbidite sequence, inferred by Dalziel et al. (1975) to be derived from the continental
143 margin.

144 Volcanic arc rocks are restricted to Annenkov Island and Pickersgill Islands (Fig. 2) to the
145 west of South Georgia. The units exposed are distinct to the lithologies of the main island. The
146 Annenkov Island Formation is formed of andesitic tuffs and breccias that have a total
147 thickness of almost 2 km (Pettigrew, 1981) and are probably Cretaceous in age (Dalziel et al.,
148 2021).

149 A potential facies equivalent of the Annenkov Island volcanic rocks is the Ducloz Head
150 Formation (Fig. 2) consisting of massive volcaniclastic breccias and interbedded tuffs,
151 although Storey (1983) also raised the possibility that components of it may be related to the
152 Sandebugten Formation. Another potentially related metasedimentary succession identified
153 as the Cooper Bay Formation is restricted to the southeast corner of the island and is a likely
154 facies variation of the Cumberland Bay Formation (Clayton, 1982).

155 Magmatic rocks have a limited areal extent across South Georgia, with the main
156 concentration cropping out in the southeast of the island along the Cooper Bay shear zone,
157 Larsen Harbour, Smaaland Cove and outlying islands (Fig. 2). Several of the granitoid plutons
158 have been dated (Mukasa and Dalziel, 1996; Curtis et al., 2010) and have yielded Middle–Late
159 Jurassic (ca. 160–150 Ma) U–Pb zircon ages from the Cooper Bay shear zone, Larsen Harbour
160 Complex and Smaaland Cove intrusive suite. Earlier geochronology on granitoid rocks by
161 Tanner and Rex (1979) yielded Rb–Sr and K–Ar ages from the Early Jurassic to mid-Cretaceous,
162 but with concerns over reliability.

163

164 **3. Sample selection**

165
166 Six samples (British Antarctic Survey archive collection) from the Drygalski Fjord Complex
167 of South Georgia were selected for detrital zircon provenance analysis; four from the
168 basement Salomon Glacier Formation (M.2022.1a, M.1683CMB2.12, M.2025.3, M.2042.1d),
169 one from the Cooper Island Formation (M.4131.15), and one undifferentiated sample
170 (M.2171.8b). All samples are medium- to coarse-grained siliciclastic metasedimentary rocks.
171 Their location is shown in figure 2 and positional information is provided in table 1.

172
173 **4. Analytical methods**

174
175 **4.1 U-Pb zircon geochronology**
176
177 Zircon (U-Pb) geochronology was carried out at University College London and the Swedish
178 Museum of Natural History. Full analytical procedures, data (Supplementary Table S1) and
179 representative spot location images (Supplementary Fig. S1) are provided in the
180 Supplementary Material. A summary of the analytical procedures is detailed here.

181 Heavy minerals were separated from bulk sieved (<300 µm) crushed rock using standard
182 density liquid and magnetic separation procedures. Zircon-enriched extracts were mounted
183 in hard epoxy resin on glass slides and polished for analysis. Zircon crystals were typically in
184 the size range 100–180 µm, with a range of grain sizes analysed for all samples. Zircon U-Pb
185 geochronology on four of the samples (M.2022.1a, M.2025.3, M.4131.15, M.2171.8b) was
186 carried out at University College London (November 2023) using laser ablation inductively
187 coupled mass spectrometry (LA-ICP-MS) facilities (Agilent 7700 coupled to a New Wave

188 Research 193 nm excimer laser) at the London Geochronology Centre. Typical laser spot sizes
189 of 25 μm were used with a 7–10 Hz repetition rate and a fluence of 2.5 J/cm², and the outer
190 parts of the grain were analysed. Background measurement before ablation lasted 15 seconds
191 and laser ablation dwell time was 25 seconds. The external zircon standard was Plešovice,
192 which has a TIMS reference age of 337.13 \pm 0.37 Ma (Sláma et al., 2008). Standard errors on
193 isotope ratios and ages included the standard deviation of $^{206}\text{Pb}/^{238}\text{U}$ ages of the Plešovice
194 standard zircon. Time-resolved signals that record isotopic ratios with depth in each crystal
195 were processed using GLITTER 4.5, developed by the ARC National Key Centre for
196 Geochemical Evolution and Metallogeny of Continents (GEMOC) at Macquarie University and
197 CSIRO Exploration and Mining, Australia. Processing enabled filtering to remove spurious
198 signals owing to overgrowth boundaries, weathering, inclusions, or fractures. Ages were
199 calculated using the $^{206}\text{Pb}/^{238}\text{U}$ ratios for samples dated as <1.1 Ga, and the $^{207}\text{Pb}/^{206}\text{Pb}$ ratios
200 for older grains. Discordance was determined using $(^{207}\text{Pb}/^{235}\text{U} - ^{206}\text{Pb}/^{238}\text{U})/(^{206}\text{Pb}/^{238}\text{U})$ and
201 similar for $^{207}\text{Pb}/^{206}\text{Pb}$ ages.

202 At the Swedish Museum of Natural History (Stockholm), U-Pb ion-microprobe zircon
203 geochronology was carried out using a CAMECA 1280 ion microprobe at the NordSIMS facility
204 (March 2024) on two further samples (M.1683CMB2.12, M.2042.1d). The analytical method
205 closely followed Whitehouse and Kamber (2005) but differed insomuch that the oxygen ion
206 primary beam was generated using a high-brightness, radiofrequency plasma ion source
207 (Oregon Physics, Hyperion II) rather than a duoplasmatron, and a focused beam instead of
208 illuminated aperture. The 10 nA O₂[–] beam was rastered over 5x5 μm to homogenize beam
209 density, the final analytical spot size being \sim 15 μm in diameter. Sputtered secondary ions
210 introduced into the mass spectrometer were analysed using a single ion counting electron

211 multiplier over 10 cycles of data. Data were reduced using in-house developed software. The
212 power law relationship between $^{206}\text{Pb}/^{238}\text{U}^{16}\text{O}$ and $^{238}\text{U}^{16}\text{O}_2/^{238}\text{U}^{16}\text{O}$ measured from the
213 91500 standard was used to calibrate U/Pb ratios following the recommendations of Jeon and
214 Whitehouse (2015). Common-Pb corrections were applied to analyses where statistically
215 significant ^{204}Pb was detected, using the present-day terrestrial common-Pb estimate of
216 Stacey and Kramers (1975). ^{207}Pb corrected ages were calculated assuming non-radiogenic Pb
217 was from surface contamination and had an isotopic composition of modern-day average
218 terrestrial common-Pb ($^{207}\text{Pb}/^{206}\text{Pb} = 0.836$; Stacey and Kramers, 1975).

219

220 **4.2 Lu-Hf isotope analysis**

221

222 Lu-Hf isotopes were determined on just one of the samples from the Salomon Glacier
223 Formation (M.2042.1d), using the same spot location as for the U-Pb dating. The analyses
224 were determined (April 2024) on a Neptune multi-collector inductively coupled plasma-mass
225 spectrometer (MC-ICP-MS) coupled with a laser ablation system at the British Geological
226 Survey. Initial $^{176}\text{Hf}/^{177}\text{Hf}$ ratios were calculated using the U-Pb crystallisation age of each grain
227 and the results are expressed as initial ϵHf (ϵHf_i). ϵHf values were calculated using a ^{176}Lu
228 decay constant of $1.867 \times 10^{-11} \text{ y}^{-1}$ (Söderlund et al., 2004), a present-day chondritic $^{176}\text{Lu}/^{177}\text{Hf}$
229 value of 0.0336, and a $^{176}\text{Hf}/^{177}\text{Hf}$ ratio of 0.282785 (Bouvier et al., 2008). Full analytical details
230 are provided in the Supplementary Material and results are presented in the Supplementary
231 Table S2.

232

233 **5. Results**

234

235 **5.1 U-Pb detrital zircon geochronology**

236

237 The age distributions of the six analysed samples are displayed as kernel density estimator
238 plots (KDE) in figure 3. They are plotted alongside the age distributions from two samples
239 from the Cretaceous Sandebugten Formation (Carter et al., 2014) to illustrate their Permian
240 age contributions. The analysed samples have very few ages >1200 Ma (Supplementary Table
241 S1), and these are omitted from the KDE plots to better illustrate the Palaeozoic age profiles.
242 The six samples from the broader Drygalski Fjord Complex all have similar age profiles
243 characterised by prominent late Permian and Early Ordovician age peaks, and a minor
244 Devonian age peak (Fig. 3; Table 1). Each sample is also characterised by a broad range of
245 Neo- and Mesoproterozoic age zircons. However, there are also notable distinctions in the
246 age profiles, with the four samples from the Salomon Glacier Formation characterised by clear
247 age peaks at ca. 270 and ca. 470 Ma (Fig. 3; Table 1), whilst the sample from the Cooper Island
248 Formation has an older Permian age peak (ca. 283 Ma), and the sample from the
249 undifferentiated Drygalski Fjord Complex (M.2171.8b) has a younger Permian age peak (ca.
250 253 Ma) and no clearly defined Early Ordovician age peak. The two samples from the
251 Sandebugten Formation, although dominated by mid-Cretaceous and Middle Jurassic age
252 peaks also have significant late Permian and minor Early Ordovician age peaks. The late
253 Permian age peaks from the Cretaceous units are distinct, with one sample having a peak at
254 ca. 250 Ma and the other at ca. 270 Ma.

255

256 **5.2 Maximum depositional age**

257

258 In the absence of diagnostic fossil assemblage and no dateable volcanic beds, detrital
259 zircon geochronology is a valuable technique to provide an estimate on the depositional age
260 of siliciclastic rocks. We follow the approach of Vermeesch (2021), who applied the maximum
261 likelihood algorithm of Galbraith and Laslett (1993) to determine the maximum depositional
262 age (MDA). The results for the six samples from the Drygalski Fjord Complex are presented as
263 radial plots (Supplementary Fig. S2) where the minima are used to derive the MDA (Table 1).

264 The samples from the Drygalski Fjord Complex and its component formations are
265 dominated by middle to late Permian MDAs, typically in the range, 265–275 Ma (Table 1;
266 Supplementary Fig. S2). One sample (M.2022.1a) has a younger MDA of 255 ± 6 Ma and is
267 consistent with a marginally younger primary age peak. Sample M.2171.8b, from the
268 undifferentiated Drygalski Fjord Complex yields a significantly younger MDA (195 ± 6 Ma) with
269 a primary age peak of ca. 253 Ma. This sample is characterised by a significant ($n=23$) number
270 of Early Jurassic–Triassic zircon grains and may represent an episode of early Mesozoic
271 accretion and recycling that developed in West Gondwana accretionary provinces (Trouw et
272 al., 1997; Flowerdew et al., 2007; Riley et al., 2023a).

273

274 **5.3 Multi-dimensional scaling analysis**

275

276 Multi-dimensional scaling analysis (MDS) is a valuable tool to help determine which
277 sedimentary units may correlate in terms of their age profile and common source regions.
278 The samples from the Drygalski Fjord Complex (excluding M.2171.8b; see section 5.1) are
279 plotted in figure 4 in comparison to a range of middle to late Permian sedimentary successions

280 from South America, Antarctic Peninsula, East Antarctica, South Africa and the
281 Falkland/Malvinas Islands (full comparative data sources in Supplementary Table 3). All
282 samples have broadly similar age profiles dominated by a primary late Permian age peak at
283 ca. 270 Ma (Fig. 5). However, the secondary age peak at ca. 470 Ma evident from the South
284 Georgia basement unit is only pronounced for the Trinity Peninsula Group (Antarctic
285 Peninsula), the southern Cordillera Darwin and the Duque de York Complex (Patagonia). The
286 MDS plot highlights this observation, with the late Permian Salomon Glacier Formation having
287 a close relationship to the middle Trinity Peninsula Group, the southern Cordillera Darwin
288 and, to a lesser degree, the Duque de York Complex. Late Permian sedimentary units from
289 South Africa have a close relationship to sedimentary rocks from the Falkland/Malvinas
290 Islands, Theron Mountains (East Antarctica), Polarstar Formation (Ellsworth Mountains) and
291 the Erewhon Beds of the southern Antarctic Peninsula (Fig. 6A) as highlighted by Riley et al.
292 (2025). Late Permian accretionary complexes from the LeMay Group of the southern Antarctic
293 Peninsula and the Bruce Bank of the southern Scotia Sea (Fig. 6A) have a more distant
294 relationship to the metasedimentary units from South Georgia and generally lack an age
295 population at ca. 470 Ma but a more prominent Cambrian peak at ca. 530 Ma that is absent
296 from the metasedimentary units of South Georgia.

297 Overall, there is a significant overlap across all late Permian sedimentary successions from
298 West Gondwana, but the units from South Georgia, particularly the Salomon Glacier
299 Formation, share the closest relationship to the accretionary complexes from the northern
300 Antarctic Peninsula (Trinity Peninsula Group) and metasedimentary rocks of southern
301 Patagonia (Cordillera Darwin and Duque de York Complex).

302

303 **5.4 Lu-Hf isotopes**

304

305 Age-adjusted Lu-Hf isotope data complement zircon U-Pb age data to provide improved
306 controls on provenance and correlation of sedimentary units, with a common source (e.g.,
307 Riley et al., 2023b). Lu-Hf isotopic analysis was undertaken on a single sample (M.2042.1d)
308 from the Drygalski Fjord Complex (Salomon Glacier Formation) that was also analysed for U-
309 Pb geochronology. The data are plotted in figure 7A alongside data from late Permian
310 sedimentary successions from Patagonia and the northern Antarctic Peninsula. The analysed
311 sample from the Salomon Glacier Formation has late Permian ϵHf_i values in the range -5 to
312 +2. There is a broad overlap in ϵHf_i values for the late Permian age population between the
313 metasedimentary units from South Georgia, Trinity Peninsula Group and Duque de York
314 Complex. The sample from the Salomon Glacier Formation analysed for Lu-Hf isotopes
315 exhibits a closer relationship to the late Permian Trinity Peninsula Group than to the Duque
316 de York Complex, with an overlap in more juvenile values (>0), which are absent in the Duque
317 de York Complex. This close relationship is also evident in the MDS plot (Fig. 4).

318 Also plotted in figure 7 are Lu-Hf values from late Permian accretionary complex from
319 Alexander Island (LeMay Group; Riley et al., 2023b) (Fig. 7B) and the late Permian deltaic
320 sandstones of the Bay of Harbours Formation from the Falkland/Malvinas Islands (Riley et al.,
321 2025) (Fig. 7C). The Bay of Harbours Formation is correlated with the upper Balfour Formation
322 of the Karoo Basin, South Africa (Riley et al., 2025) (Fig. 4) and can be considered a proxy for
323 the late Permian Karoo Basin, for which no Lu-Hf data are available. The ϵHf_i range for the
324 LeMay Group overlaps with that of the Salomon Glacier Formation, particularly LeMay Group
325 2. The range defined by the Bay of Harbours Formation (Fig. 7C) exhibits only limited overlap

326 with the distribution of Salomon Glacier Formation data and generally lacks the more evolved
327 values (<-3) of the Salomon Glacier Formation and the Trinity Peninsula Group/Duque de York
328 Complex.

329

330 **6. Discussion**

331

332 Eagles and Eisermann (2020) examined plate kinematic reconstructions of the Scotia Sea
333 and established that only half of South Georgia's proposed translation can be readily
334 accounted for, assuming a 'starting' position in a back-arc setting adjacent to Tierra del Fuego.

335 As a consequence, they challenged existing correlations to South America based on
336 similarities in stratigraphy, tectonic setting and detrital zircon geochronology as being non-
337 unique and equally explicable through geological links to southern Africa and East Antarctica.

338 Their Early Jurassic reconstruction (Fig. 6B), which we use as an early Mesozoic proxy, places
339 South Georgia adjacent to Coats Land and the Theron Mountains of East Antarctica, and
340 adjacent to the Natal Embayment, with close links to southern Africa. Eagles and Eisermann

341 (2020) suggested the presence of a newly recognised plate ('Skytrain'; Fig. 6B) that was
342 hypothesised from sea floor architecture in the Falkland/Malvinas Basin. Their model also
343 requires a South American setting for the Falkland/Malvinas Islands and negates the
344 requirement for long distance translation of the South Georgia microcontinent.

345 In contrast, our analysis demonstrates strong evidence in favour of a connection between
346 the late Permian accretionary successions of South Georgia with the mid-late Permian
347 accretionary complexes of the northern Antarctic Peninsula and parts of Tierra del Fuego. We
348 agree with Eagles and Eisermann (2020) that the application of detrital zircon geochronology

349 for identifying exact provenance is often non-unique, particularly during periods of enhanced
350 volcanism, deposition and sediment recycling. The late Permian is such an episode, with
351 extensive silicic (zircon-rich) volcanism (e.g., Choiyoi Province), widespread accretionary
352 complexes (e.g., Madre de Dios) and extensive sediment recycling and deposition in the
353 hinterland (e.g., Karoo Basin). However, our analysis of the U-Pb dataset from the late
354 Permian metasedimentary units from South Georgia, supported by Lu-Hf isotopes, highlights
355 several aspects in the data that argue against a direct connection to East Antarctica and South
356 Africa, but strongly favour a close relationship to the northern Antarctic Peninsula and parts
357 of Tierra del Fuego. The maximum depositional age of ca. 270 Ma of the Salomon Glacier
358 Formation and other parts of the Drygalski Fjord Complex (Table 1), as well as the accretionary
359 complexes of the Antarctic Peninsula and Patagonia, is also ubiquitous in East Antarctica,
360 Karoo Basin and the southern Antarctic Peninsula (Riley et al., 2025). However, a critical
361 aspect of the age profile from the Salomon Glacier Formation and Drygalski Fjord Complex is
362 the significant secondary age peak at ca. 470 Ma that is essentially absent from the hinterland
363 successions in South Africa and East Antarctica, which are instead characterised by a
364 secondary age peak at ca. 530 Ma, that is absent in South Georgia (Fig. 5). This Cambrian age
365 peak may correlate with sources from granitoids associated with the Ross Orogen, or more
366 likely represent recycling from early Palaeozoic sedimentary successions with more distal
367 Gondwana sources. The ca. 470 Ma event is related to the widespread Famatinian magmatic
368 arc and orogeny of South America (Rapela et al., 2018; Otamendi et al., 2020) that also
369 extended via northeastern Patagonia (Pankhurst et al., 2014) into eastern Graham Land of
370 the northern Antarctic Peninsula (Riley et al., 2012, 2023b). The age signature of the
371 Ordovician Famatinian arc is evident in the recycled component of the late Permian

372 metasedimentary rocks of Patagonia (Duque de York Complex, Cordillera Darwin) and the
373 northern Antarctic Peninsula, and indicates relative proximity to a source region. Lu-Hf
374 isotopes also support a close relationship between the Salomon Glacier Formation of South
375 Georgia and the mid-Permian Trinity Peninsula Group of the Antarctic Peninsula, as well as
376 components of the Duque de York Complex (Fig. 7).

377 Overall, the data support a close association between the South Georgia microcontinent
378 and the northern Antarctic Peninsula, with a near-neighbour relationship in age profiles and
379 Lu-Hf isotopes between the mid-late Permian accretionary complex of the Trinity Peninsula
380 Group and the accretionary complex of the Salomon Glacier Formation. The Duque de York
381 Complex is also likely to be relatively close, but we support a closer location to the Cordillera
382 Darwin (Fig. 6A), particularly if a South Georgia location adjacent to the Isla de los Estados
383 (Staten Island; Fig. 1) is favoured (Dalziel et al., 2021). A detrital zircon age profile for a late
384 Permian metasedimentary unit from the southern Cordillera Darwin (FO0642; Hervé et al.,
385 2010) is plotted in figures 4 and 5 and exhibits a prominent mid-late Permian age peak, and
386 also a significant Early Ordovician age peak likely indicating derivation from the Famatinian
387 arc or recycled unit.

388 Hervé et al. (2010) suggested that the Cordillera Darwin metamorphic complex has a
389 distinct geological history from elsewhere in Patagonia and lies on the Scotia Plate and not
390 the South American Plate. This scenario was supported by Riley et al. (2022) who developed
391 a new dynamic plate model to demonstrate that the Cordillera Darwin metamorphic complex
392 could have originated on the Antarctic Plate before translation to the Scotia Plate in the
393 Eocene, along with the crustal blocks of the South Scotia Ridge (Fig. 1). Close paleo-location
394 of the Cordillera Darwin, northern Antarctic Peninsula and the South Georgia microcontinent

395 is supported by their overlap in the MDS plot (Fig. 4), although this only represents late
396 Permian successions.

397 Placing South Georgia adjacent to the northern Antarctic Peninsula and Cordillera Darwin,
398 particularly with a rotated Antarctic Peninsula, may negate the requirement for such lengthy
399 lateral translation for the South Georgia microcontinent (Eagles and Eisermann, 2020), but
400 still satisfies geological and tectonic correlations to the Staten Embayment (Dalziel et al.,
401 2021). Famatinian-age (ca. 470 Ma) zircons in South Georgia, Cordillera Darwin and the
402 northern Antarctic Peninsula all suggest a nearby source. The ϵ_{Hf_i} data (Fig. 7A) from the
403 Salomon Glacier Formation for the Ordovician-age zircons (typically -5 to 0) are also
404 consistent with the values reported by Rapela et al. (2018) from the Famatinian magmatic
405 province. The Famatinian magmatic arc is generally considered to only extend as far south as
406 the North Patagonian Massif (Pankhurst et al., 2014; Rapela et al., 2018), but with well-
407 defined age peaks in the recycled sedimentary record of the northern Antarctic Peninsula
408 (Riley et al., 2023b), a more southerly extent is likely (Castillo et al., 2020). Isolated outcrops
409 of Early Ordovician magmatism in the north-eastern Antarctic Peninsula (Riley et al., 2012)
410 confirm this.

411

412 7. Conclusions

413

414 Using U-Pb and Lu-Hf detrital zircon analysis we demonstrate that the late Permian
415 accretionary complex of South Georgia (Drygalski Fjord Complex) has a close association in
416 depositional age and common source to metasedimentary units from the northern Antarctic
417 Peninsula, and also the southern Cordillera Darwin and Duque de York Complex of southern

418 Patagonia. The mid-late Permian is dominated by widespread accretionary complexes and
419 recycled sedimentary successions across West Gondwana, which are all characterised by
420 prominent late Permian age signals (ca. 260–270 Ma). The late Permian units from South
421 Georgia, the northern Antarctic Peninsula and southern Patagonia are also characterised by
422 a significant secondary age peak at ca. 470 Ma, correlating with the Early Ordovician
423 Famatinian magmatic arc.

424 Although mid-late Permian units from South Africa, Falkland/Malvinas Islands and East
425 Antarctica all have similar maximum depositional ages to the accretionary complexes of South
426 Georgia, they lack a significant secondary age peak at ca. 470 Ma and are instead
427 characterised by a mid-Cambrian age peak at ca. 530 Ma, typical of Cambrian recycled
428 material of East Antarctica.

429 We favour a late Permian–early Mesozoic paleo-location of South Georgia adjacent to the
430 northern Antarctic Peninsula and the Cordillera Darwin, all located on the Antarctic Plate,
431 prior to closure of the Rocas Verdes Basin and subsequent translation of South Georgia and
432 Cordillera Darwin to the Scotia Plate.

433 We rule out close links between South Georgia and South Africa/East Antarctica as
434 proposed by Eagles and Eisermann (2020) in their Skytrain Plate model.

435
436 **Acknowledgements**

437 This study is part of the British Antarctic Survey Polar Science for a Sustainable Planet
438 programme, funded by the Natural Environmental Research Council. The original samples
439 were collected by Bryan Storey and Charles Bell and their detailed field observations were
440 critical for our interpretations. Mark Evans prepared samples for zircon separation, Heejin

441 Jeon, Andreas Karlsson and Kerstin Lindén provided support at the NordSIMS facility
442 (supported by the Swedish Research Council infrastructure grant 2021-00276) and Ben Evans
443 assisted with analyses at UCL. This paper has benefited from the helpful contributions of
444 Joaquín Bastías-Silva, Daniel Bertin, Paula Castillo, Josh Malone, Bob Pankhurst and Phil Stone.
445 This is NordSIMS contribution number 809.

446

447 **Data availability**

448 The data that support this research are all available as supplementary files linked to this
449 article. Full datasets are also hosted at the British Antarctic Survey's Polar Data Centre
450 <https://doi.org/10.5285/270714e6-f141-4c01-8a13-2bdfaca80ced>

451

452 **References**

453

454 Barbeau, D.L.; Davis, J.T.; Murray, K.E.; Valencia, V.; Gehrels, G.E.; Zahid, K.M.; Gombosi, D.J.
455 2010. Detrital-zircon geochronology of the metasedimentary rocks of north-western
456 Graham Land. Antarctic Science 22: 65-78.

457 Beaver, D.G.; Kent, D.V.; Dalziel, I.W.D. 2022. Paleomagnetic constraints from South Georgia
458 on the tectonic reconstruction of the Early Cretaceous Rocas Verdes marginal basin system
459 of southernmost South America. Tectonics 41: e2021TC006990.

460 Bouvier, A.; Vervoort, J.D.; Patchett, P.J. 2008. The Lu–Hf and Sm–Nd isotopic composition of
461 CHUR: constraints from unequilibrated chondrites and implications for the bulk
462 composition of terrestrial planets: Earth and Planetary Science Letters 273 (1): 8-57.

463 Carter, A.; Curtis, M.; Schwanethal, J. 2014. Cenozoic tectonic history of the South Georgia
464 microcontinent and potential as a barrier to Pacific-Atlantic through flow. *Geology* 42:
465 295–298. <https://doi.org/10.1130/G35091.1>.

466 Castillo, P.; Fanning, C.M.; Hervé, F.; Lacassie, J.P. 2016. Characterization and tracing of
467 Permian magmatism in the south-western segment of the Gondwanan margin; U–Pb age,
468 Lu–Hf and O isotopic compositions of detrital zircons from metasedimentary complexes of
469 northern Antarctic Peninsula and western Patagonia. *Gondwana Research* 36: 1–13,
470 doi:10.1016/j.gr.2015.07.014.

471 Castillo, P.; Fanning, C.M.; Riley, T.R. 2020. Zircon O and Hf isotope constraints on the genesis
472 of Permian–Triassic magmatic and metamorphic rocks in the Antarctic Peninsula and
473 correlations with Patagonia. *Journal of South American Earth Sciences* 104: 10 pp.
474 10.1016/j.jsames.2020.102848

475 Clayton, R.A.S. 1982. A preliminary investigation of the Geochemistry of greywackes from
476 South Georgia. *British Antarctic Survey Bulletin* 51: 89–109.

477 Craddock, J.P.; Fitzgerald, P.; Konstantinou, A.; Nereson, A.; Thomas, R.J. 2017. Detrital zircon
478 provenance of upper Cambrian-Permian strata and tectonic evolution of the Ellsworth
479 Mountains, West Antarctica. *Gondwana Research* 45: 191–207,
480 doi:10.1016/j.gr.2016.11.011.

481 Curtis, M.L. 2011. Geological Map of South Georgia (1:250 000 scale). In: BAS GEOMAP2
482 Series, Sheet 4. British Antarctic Survey, Cambridge, UK.

483 Curtis, M.L.; Flowerdew, M.J.; Riley, T.R.; Whitehouse, M.J.; Daly, J.S. 2010. Andean sinistral
484 transpression and kinematic partitioning in South Georgia. *Journal of Structural Geology*.
485 32: 464–477.

486 Dalziel, I.W.D.; Dott, R.H.; Winn, R.D.; Bruhn, R.L. 1975. Tectonic relations of South Georgia
487 Island to the Southernmost Andes. *Geological Society of America Bulletin* 86: 1034–1040.

488 Dalziel, I.W.D.; Macdonald, D.I.M.; Stone, P.; Storey, B.C. 2021. South Georgia microcontinent:
489 Displaced fragment of the southernmost Andes. *Earth Science Reviews* 220:
490 <https://doi.org/10.1016/j.earscirev.2021.103671>

491 Eagles, G. 2010. South Georgia and Gondwana's Pacific Margin: Lost in translation? *Journal of*
492 *South American Earth Sciences* 30(2): 65–70.

493 Eagles, G.; Eisermann, H. 2020. The Skytrain plate and tectonic evolution of southwest
494 Gondwana since Jurassic times. *Scientific Reports* 10: 1-17, doi:10.1038/s41598-020-
495 77070-6.

496 Elliot, D.H.; Fanning, C.M.; Laudon, T.S. 2016. The Gondwana Plate margin in the Weddell Sea
497 sector: Zircon geochronology of Upper Paleozoic (mainly Permian) strata from the
498 Ellsworth Mountains and eastern Ellsworth Land, Antarctica. *Gondwana Research* 29: 234–
499 247, doi:10.1016/j.gr.2014.12.001.

500 Fanning, C.M.; Hervé, F.; Pankhurst, R.J.; Rapela, C.W.; Kleiman, L.E.; Yaxley, G.M.; Castillo, P.
501 2011. Lu–Hf isotope evidence for the provenance of Permian detritus in accretionary
502 complexes of western Patagonia and the northern Antarctic Peninsula region. *Journal of*
503 *South American Earth Sciences* 32 (4): 485–496.

504 Flowerdew, M.J.; Daly, J.S.; Riley, T.R. 2007. New Rb-Sr mineral ages temporally link plume
505 events with accretion at the margin of Gondwana. *A Keystone in a Changing World – Online*
506 *Proceedings of the 10th ISAES*, edited by A.K. Cooper and C.R. Raymond et al., USGS Open-
507 File Report 2007-1047, Short Research Paper 012, 4 p.; doi:10.3133/of2007-1047.srp012.

508 Flowerdew, M.J.; Tyrell, S.; Riley, T.R.; Whitehouse, M.J.; Mulvaney, R.W.; Leat, P.T.;
509 Marschall, H.R. 2012. Distinguishing East and West Antarctic sediment sources using the
510 Pb isotope composition of detrital K feldspar. *Chemical Geology* 292-293: 88-102.

511 Galbraith, R.; Laslett, G. 1993. Statistical models for mixed fission track ages. *Nucl. Tracks
512 Radiat. Meas.*: 21 (4), 459-470.

513 Hervé, F.; Fanning, C.M.; Pankhurst, R.J. 2003. Detrital zircon age patterns and provenance of
514 the metamorphic complexes of southern Chile. *Journal of South American Earth Sciences*
515 16: 107-123.

516 Hervé, F.; Fanning, C.M.; Pankhurst, R.J.; Mpodozis, C.; Klepeis, K.; Calderón, M.; Thomson,
517 S.N. 2010. Detrital zircon SHRIMP U-Pb age study of the Cordillera Darwin Metamorphic
518 Complex of Tierra del Fuego: Sedimentary sources and implications for the evolution of the
519 Pacific margin of Gondwana. *Journal of the Geological Society* 167: 555-568.

520 Jeon, H.; Whitehouse, M.J. 2015. A critical evaluation of U-Pb calibration schemes used in
521 SIMS zircon geochronology. *Geostandards and Geoanalytical Research* 39: 443-452.

522 Livermore, R.; McAdoo, D.; Marks, K.M. 1994. Scotia Sea tectonics from high-resolution
523 satellite gravity. *Earth and Planetary Science Letters* 123: 255-268.

524 Macdonald, D.I.M., 1982. Palaeontology and ichnology of the Cumberland Bay Formation,
525 South Georgia. *British Antarctic Survey Bulletin* 57: 1-14

526 Macdonald, D.I.M.; Storey, B.C.; Thomson, J.W. 1987. South Georgia, BAS GEOMAP Series,
527 Sheet 1, 1:250,000, Geological Map and Supplementary Text. British Antarctic Survey,
528 Cambridge, 63 pp.

529 Mair, B.F. 1987. The Geology of South Georgia: VI. Larsen Harbour Formation. *British Antarctic
530 Survey Scientific Reports* No. 111, 60 pp.

531 Mukasa, S.B.; Dalziel, I.W.D., 1996. Southernmost Andes and South Georgia Island, North
532 Scotia Ridge: zircon U-Pb and muscovite $^{40}\text{Ar}/^{39}\text{Ar}$ age constraints on tectonic evolution of
533 Southwestern Gondwanaland. *Journal of South American Earth Sciences* 9: 349-365.

534 Otamendi, J.E.; Cristofolini, E.A.; Morosini, A.; Armas, P.; Tibaldi, A.M.; Camilletti, G.C. 2020.
535 The geodynamic history of the Famatinian arc, Argentina: A record of exposed geology over
536 the type section (latitudes 27°- 33° south). *Journal of South American Earth Sciences* 100:
537 102558. <https://doi.org/10.1016/j.jsames.2020.102558>

538 Pankhurst, R.J.; Rapela, C.W.; López de Luchi, M.G.; Rapalini, A.E.; Fanning, C.M.; Galindo, C.,
539 2014. The Gondwana connections of northern Patagonia. *Journal of the Geological Society*
540 171(3): 313-328.

541 Pettigrew, T.H. 1981. The geology of Annenkov Island. *British Antarctic Survey Bulletin* 53:
542 213–254

543 Rapela, C.W.; Pankhurst, R.J.; Casquet, C.; Dahlquist, J.A.; Fanning, C.M.; Baldo, E.G.; Galindo,
544 C.; Alasino, P.H.; Ramacciotti, C.D.; Verdecchia, S.O.; Murra, J.A.; Basei, M.A.S. 2018. A
545 review of the Famatinian Ordovician magmatism in southern South America: evidence of
546 lithosphere reworking and continental subduction in the early proto-Andean margin of
547 Gondwana. *Earth-Science Reviews* 187: 259–285.

548 Riley, T.R.; Flowerdew, M.J.; Whitehouse, M.J. 2012. U-Pb ion-microprobe zircon
549 geochronology from the basement inliers of eastern Graham Land, Antarctic Peninsula.
550 *Journal of the Geological Society* 169: 381-393.

551 Riley, T.R.; Carter, A.; Leat, P.T.; Burton-Johnson, A.; Bastías, J.; Spikings, R.A.; Tate, A.J.;
552 Bristow, C.S. 2019. Geochronology and geochemistry of the northern Scotia Sea: a revised

553 interpretation of the North and West Scotia ridge junction. *Earth and Planetary Science*
554 *Letters* 518: 136–147.

555 Riley, Teal R.; Carter, Andrew; Burton-Johnson, Alex; Leat, Philip T.; Hogan, Kelly A.; Bown,
556 Paul R. 2022. Crustal block origins of the South Scotia Ridge. *Terra Nova* 34: 8 pp.
557 10.1111/ter.12613

558 Riley, T.R.; Millar, I.L.; Carter, A.; Flowerdew, M.J.; Burton-Johnson, A.; Bastías, J.; Storey, C.D.;
559 Castillo, P.; Chew, D.; Whitehouse, M.J. 2023a. Evolution of an accretionary complex LeMay
560 Group and terrane translation in the Antarctic Peninsula. *Tectonics*. 10.1029/2022TC007578.

561 Riley, Teal R.; Burton-Johnson, Alex; Flowerdew, Michael J.; Poblete, Fernando; Castillo, Paula;
562 Hervé, Francisco; Leat, Philip T.; Millar, Ian L.; Bastias, Joaquin; Whitehouse, Martin J.
563 2023b. Palaeozoic – Early Mesozoic geological history of the Antarctic Peninsula and
564 correlations with Patagonia: Kinematic reconstructions of the proto-Pacific margin of
565 Gondwana. *Earth-Science Reviews* 236: 10.1016/j.earscirev.2022.104265

566 Riley, Teal R.; Carter, Andrew; Hunter, Morag. A.; Millar, Ian L.; Flowerdew, Michael J.; Curtis,
567 Michael L.; Hodgson, Dominic A. 2025. Provenance and correlation of Permian successions from
568 the Falkland/Malvinas Islands with West Gondwana: implications for a Natal Embayment
569 palaeo-location. *Journal of the Geological Society* 182 (4): 10.1144/jgs2024-282

570 Sláma, J.; Košler, J.; Condon, D.J.; Crowley, J.L.; Gerdes, A.; Hanchar, J.M.; Horstwood, M.S.A.;
571 Morris, G.A.; Nasdala, L.; Norberg, N.; Schaltegger, U.; Schoene, B.; Tubrett, M.N.;
572 Whitehouse, M.J. 2008. Plešovice zircon - a new natural reference material for U–Pb and
573 Hf isotopic microanalysis. *Chemical Geology* 249 (1–2): 1–35.

574 Söderlund, U.; Patchett, P.J.; Vervoort, J.D.; Isachsen, C.E. 2004. The ^{176}Lu decay constant
575 determined by Lu–Hf and U–Pb isotope systematics of Precambrian mafic intrusions: Earth
576 and Planetary Science Letters 219 (3): 311-324.

577 Stacey, J.S.; Kramers, J.D. 1975. Approximation of terrestrial lead evolution by a two-stage
578 model. Earth and Planetary Science Letters 26: 207-221.

579 Storey, B.C. 1983. The geology of South Georgia: V. Drygalski Fjord Complex. British Antarctic
580 Survey Scientific Reports 107: 88 pp.

581 Tanner, P.W.G.; Rex, D.C. 1979. Timing of events in an Early Cretaceous Island arc marginal
582 basin system on South Georgia. Geological Magazine 116: 167-179.

583 Trouw, R.A.J.; Passchier, C.W.; Simoes, L.S.A.; Andreis, R.R.; Valeriano, C.M. 1997. Mesozoic
584 tectonic evolution of the South Orkney Microcontinent, Scotia arc, Antarctica. Geological
585 Magazine 134: 383-401.

586 Vermeesch, P. 2013. Multi-sample comparison of detrital age distributions. Chemical Geology
587 341: 140-146.

588 Vermeesch, P. 2018. IsoplotR: a free and open toolbox for geochronology. Geoscience
589 Frontiers 9: 1479-1493. <https://doi.10.1016/j.gsf.2018.04.001>.

590 Vermeesch, P. 2021. Maximum depositional age estimation revisited. Geoscience Frontiers
591 12: 843-850.

592 Viglietti, P.A.; Frei, D.; Rubidge, B.S.; Smith, R.M.H. 2018. U-Pb detrital zircon dates and
593 provenance data from the Beaufort Group (Karoo Supergroup) reflect sedimentary
594 recycling and air-fall tuff deposition in the Permo-Triassic Karoo foreland basin. Journal of
595 African Earth Sciences 143: 59–66, doi:10.1016/j.jafrearsci.2017.11.006.

596 Whitehouse, M.J.; Kamber, B.S. 2005. Assigning dates to thin gneissic veins in high-grade
597 metamorphic terranes: A cautionary tale from Akilia, southwest Greenland. *Journal of*
598 *Petrology* 46: 291-318.

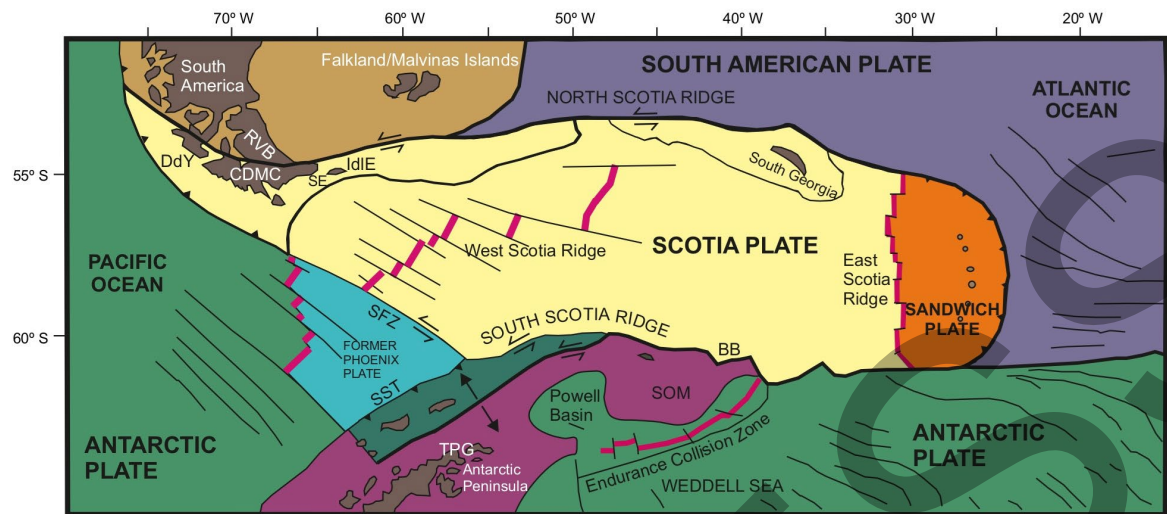
599

600

601

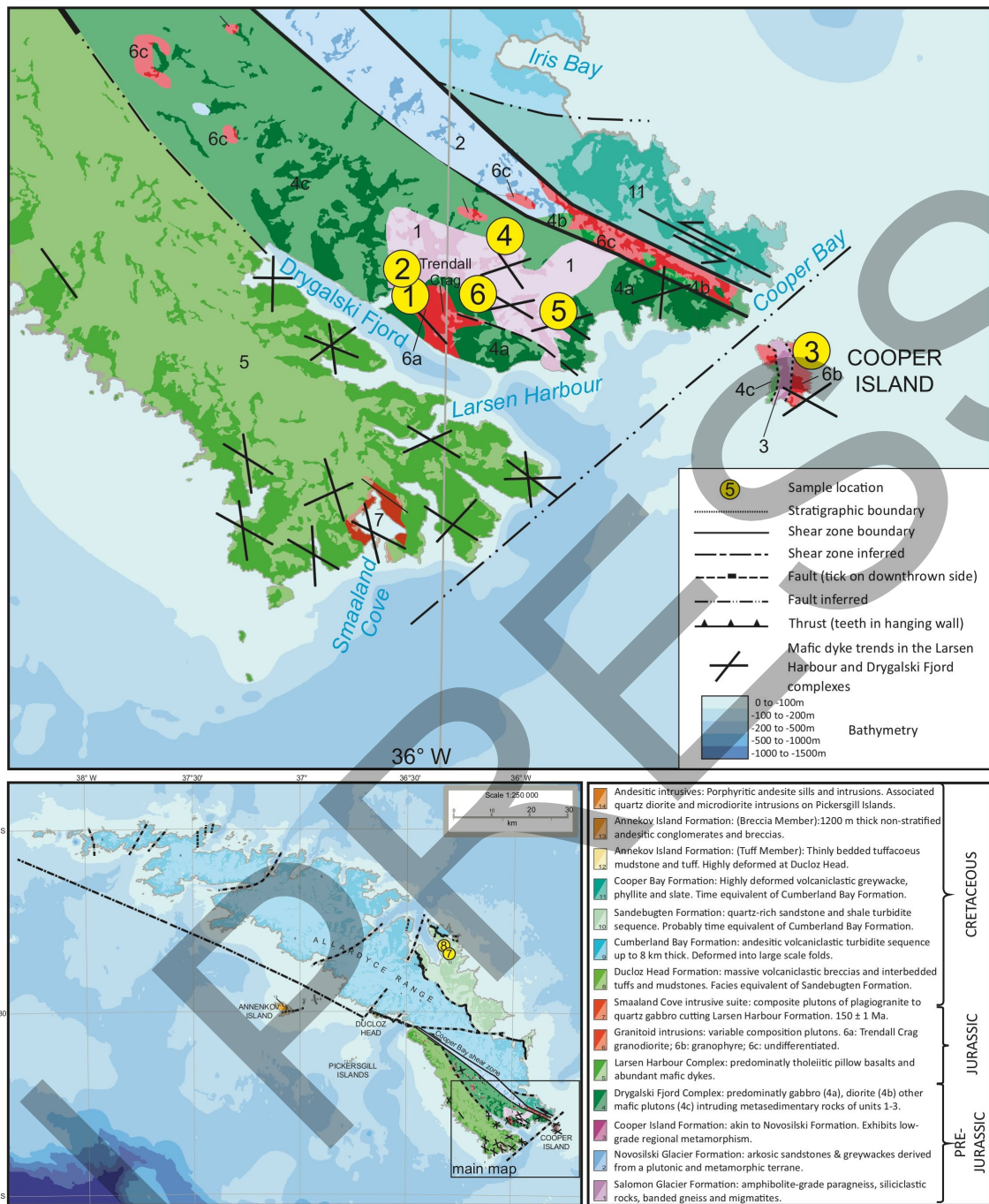
IN PRESS

602 List of Figures

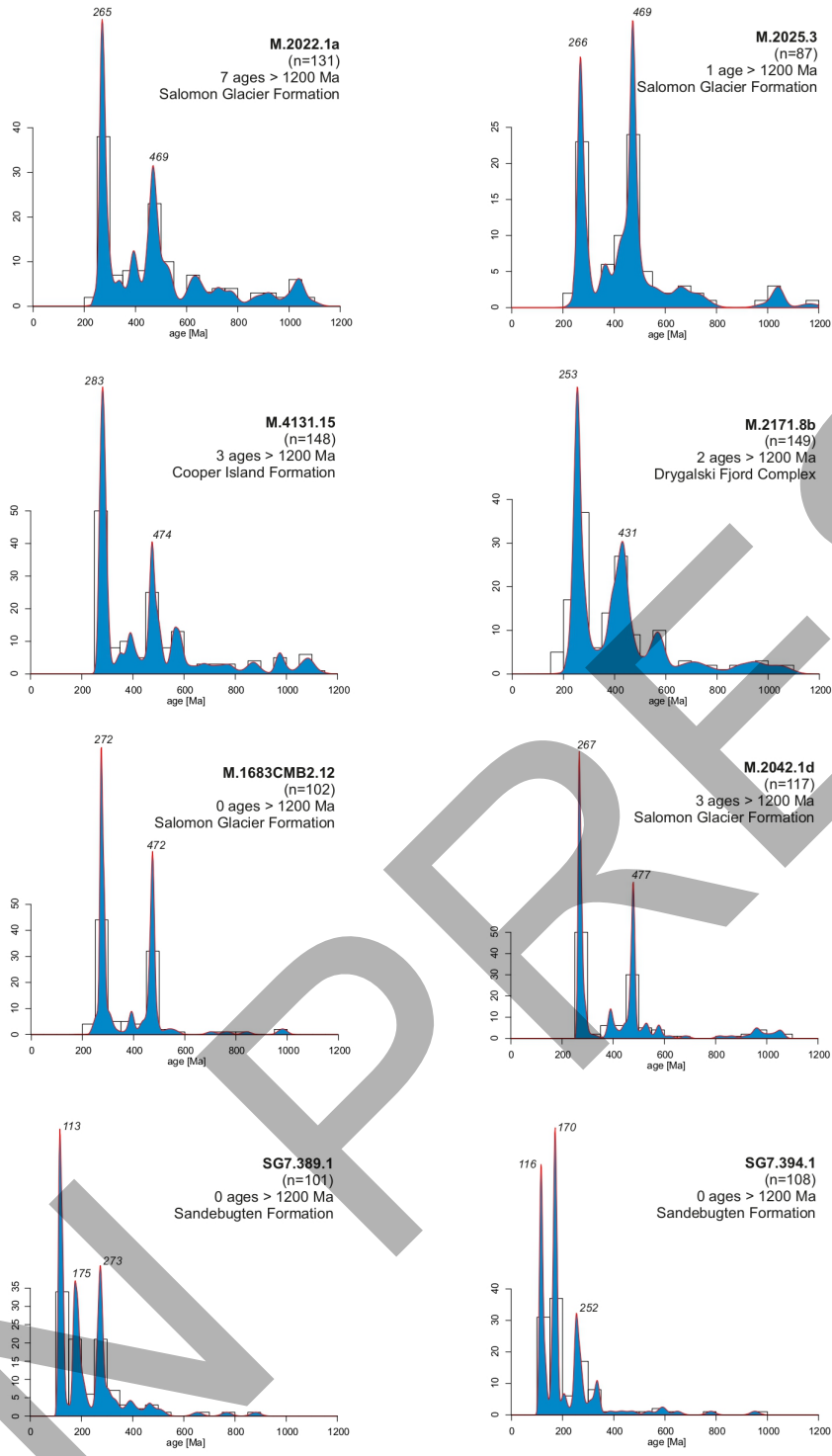


603

604 FIG. 1. Tectonic setting of the Scotia Sea (adapted from Riley et al., 2022). BB: Bruce Bank;
605 CDMC: Cordillera Darwin metamorphic complex; DdY: Duque de York Complex; IdIE: Isla de
606 los Estados (Staten Island); RVB: Rocas Verdes Basin; SE: Staten Embayment; SFZ: Shackleton
607 Fracture Zone; SOM: South Orkney microcontinent; SST: South Shetland trough; TPG: Trinity
608 Peninsula Group.



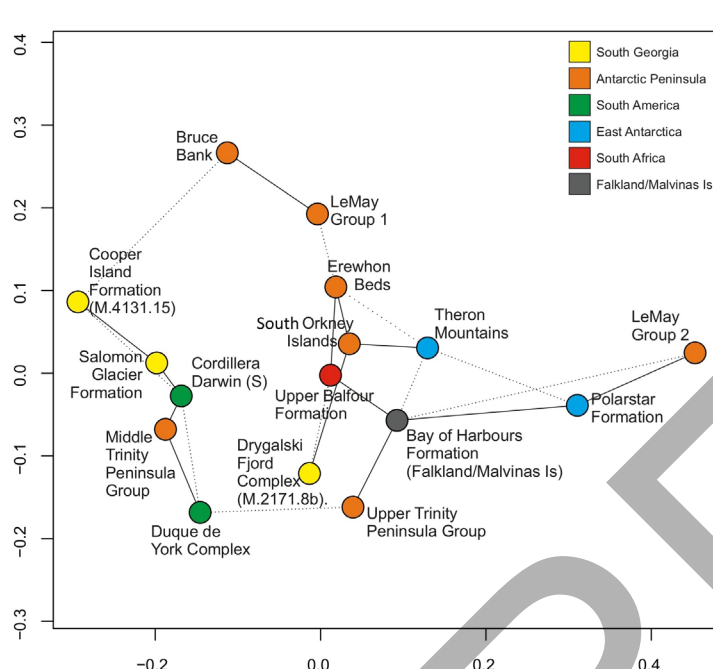
609
610 FIG. 2. Geological map of South Georgia, modified from Curtis (2011). Darker areas show the
611 extent of rock outcrop, with the paler areas showing inferred geology. Sample locations (see
612 Table 1 for precise positional information): 1. M.2022.1a; 2. M.2025.3; 3. M.4131.15; 4.
613 M.2171.8b; 5. M.1683CMB2.12; 6. M.2042.1d; 7. SG7.389.1 (54.33670° S, 36.32457° W); 8.
614 SG7.394.1 (54.33611° S, 36.34062° W).



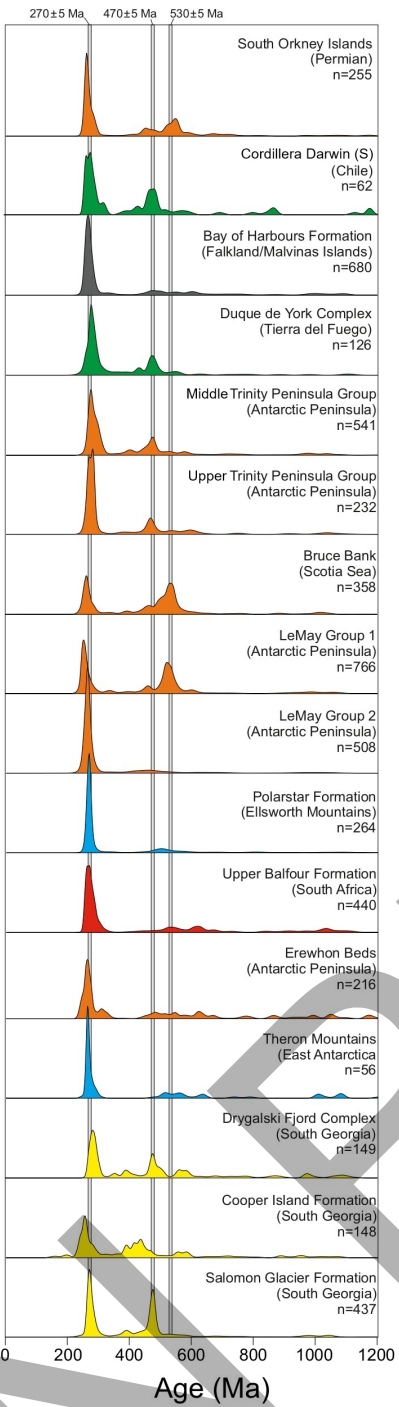
615

616 FIG. 3. Kernel density estimator (KDE) plots (Vermeesch, 2013) of U-Pb detrital zircon ages for
 617 metasedimentary rocks from the Drygalski Fjord Complex (this study) and from the
 618 Sandebugten Formation (Carter et al., 2014). Full datasets are available in Supplementary

619 Table 1. Analytical details in Supplementary Material. Bandwidths for all plotted samples are
 620 50 Myr. The area under the KDE plots is not normalised and an adaptive kernel bandwidth
 621 was applied. Sample locations as shown in figure 2.

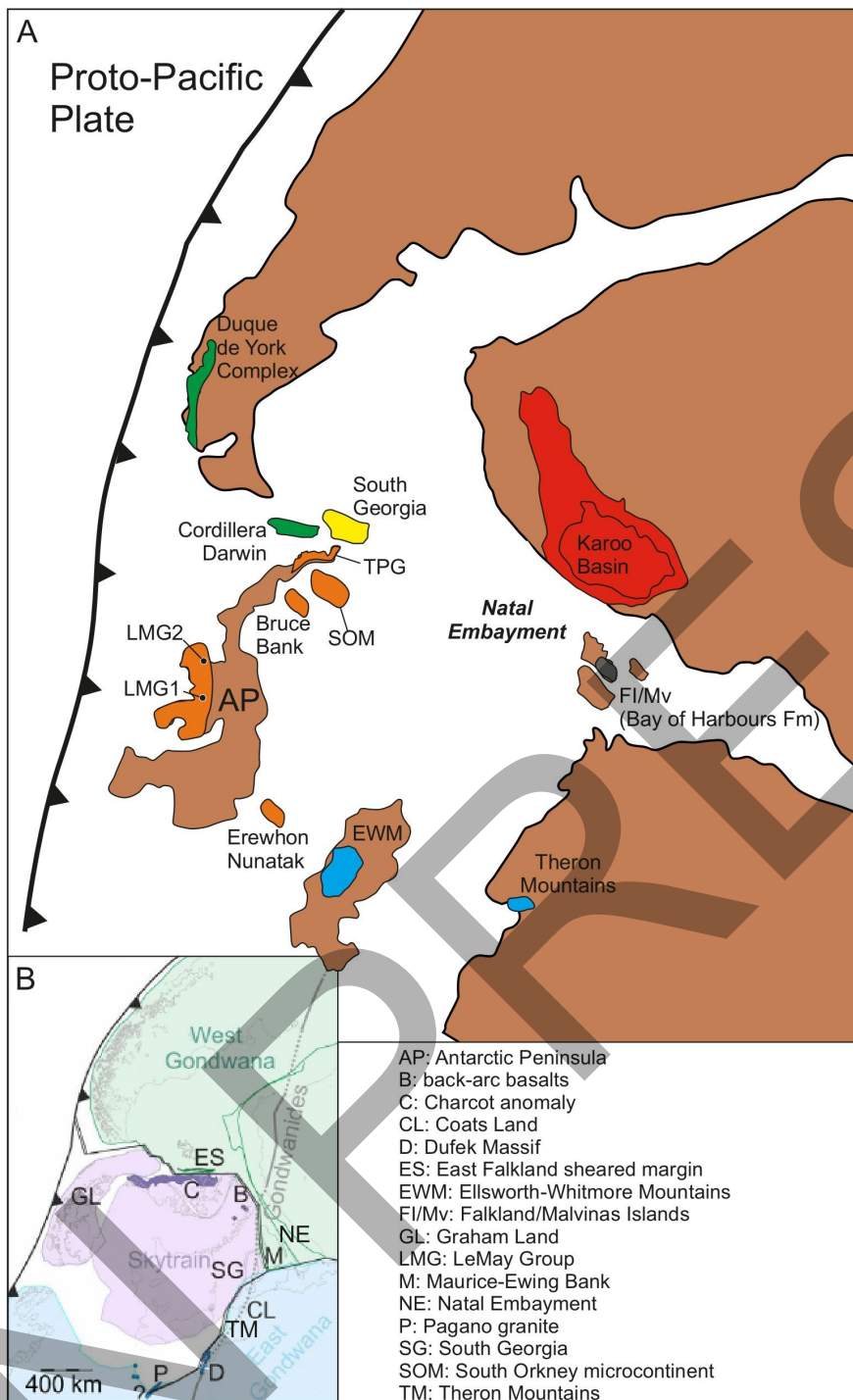


622
 623 FIG. 4. Multidimensional scaling maps (MDS; Vermeesch, 2013, 2018) for late Permian
 624 sedimentary units from West Gondwana. MDS plots compare the complete age spectra in
 625 dissimilar samples calculated using the Kolmogorov-Smirnov statistic with any two points
 626 plotting closer together if they are more similar. Nearest (solid) and secondary (dashed)
 627 neighbour lines are shown. The axis scales are dimensionless and have no physical meaning.
 628 Data from Hervé et al. (2003, 2010), Barbeau et al. (2010), Flowerdew et al. (2012), Elliot et
 629 al. (2016), Castillo et al. (2016), Carter et al. (2017), Craddock et al. (2017), Viglietti et al.
 630 (2018), Nelson and Cottle (2019), and Riley et al. (2022, 2023a,b, 2025). A detailed list of late
 631 Permian data sources is provided in Supplementary Table S3. Salomon Glacier Formation
 632 (M.2022.1a, M.2025.3, M.2042.1d, M.1683CMB2.12); Cooper Island Formation (M.4131.15);
 633 Drygalski Fjord Complex (M.2171.8b).



634

635 FIG. 5. U-Pb age stacked (KDE) plots for mid-late Permian samples. Grey bars represent
 636 significant zircon peaks at ca. 270 ± 5 Ma, ca. 470 ± 5 Ma and ca. 530 ± 5 Ma. Data sources as in
 637 figure 4. The area under the KDE plots is normalised and an adaptive kernel bandwidth was
 638 applied. Data sources are provided in Supplementary Table S3.

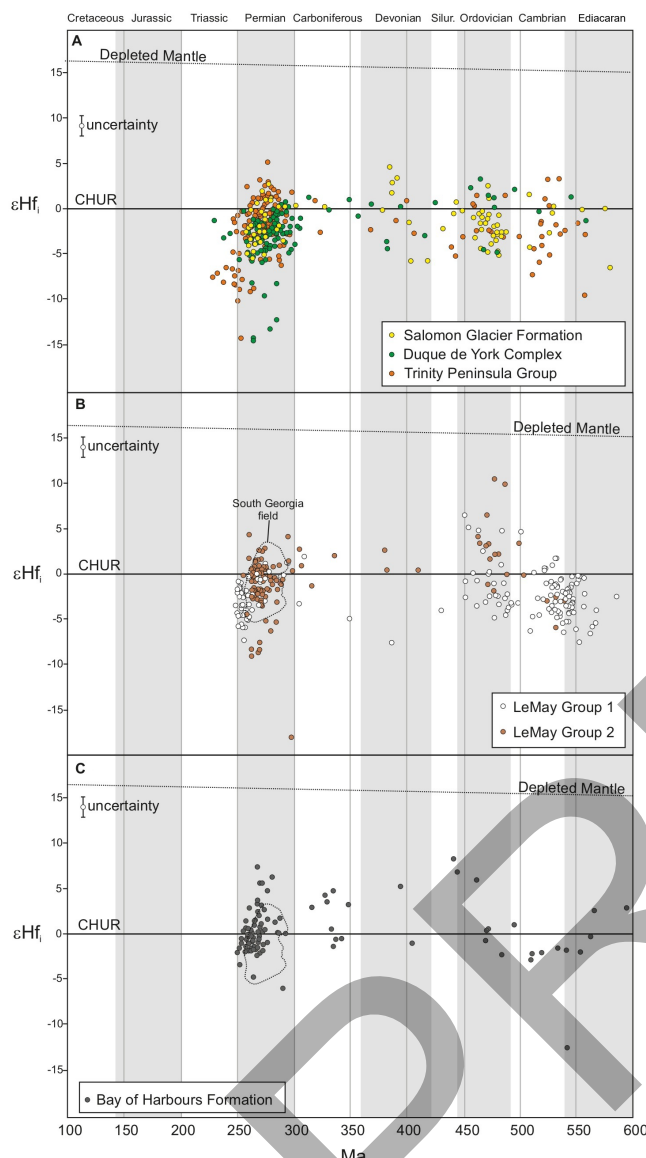


639

640 FIG. 6. A. Late Permian reconstruction of West Gondwana, adapted from Riley et al. (2025).

641 B. Early Mesozoic plate reconstruction from Eagles and Eisermann (2020) showing the

642 putative Skytrain Plate (purple domain).



643

644 FIG. 7. U-Pb zircon ages ($^{238}\text{U}/^{206}\text{Pb}$) versus initial ϵHf values for zircon grains from late
 645 Permian metasedimentary successions examined as part of this study. Vertical grey and white
 646 bars represent geological periods. **A.** Drygalski Fjord Complex (South Georgia), Trinity
 647 Peninsula Group (Antarctic Peninsula), Duque de York Complex (Patagonia) (Barbeau et al.,
 648 2010; Fanning et al., 2011; Castillo et al., 2016; this study). **B.** LeMay Group accretionary
 649 complex (Riley et al. 2023a). **C.** Bay of Harbours Formation (Riley et al., 2025). Full Lu-Hf
 650 dataset is provided in Supplementary Table S2. Dashed lines in B and C encompass the late
 651 Permian South Georgia sample data shown in A. CHUR: Chondritic uniform reservoir.